Jain et al. *NPG Asia Materials* (2026)18:16
https://doi.org/10.1038/s41427-026-00644-9

NPG Asia Materials

ARTICLE Open Access

Superior capacity behaviour of mesoporous, edge-free carbon materials with ionogel electrolytes

Amrita Jain[1], Daniel Moreno-Rodríguez[2], Shinichiroh Iwamura[3], Hirotomo Nishihara[3], Robert K. Szilagyi[4], Monika Michalska[5] and Eva Scholtzova[6]

Abstract

The design and optimisation of electrode and electrolyte materials to tune the properties of capacitors is a complex task with often unexpected outcomes. In this work, we assessed the electrochemical performance of a new carbon material, Graphene MesoSponge® (GMS), in combination with a flexible electrolyte, ionogel built from polyvinylalcohol polymer matrix and ionic liquid (IL) with ethylmethylimidazolium cations and bisulfate anions. From the electrochemical characterisations employing cyclic voltammetry, electrochemical impedance spectroscopy, and galvanostatic charge-discharge, we established the superior performance of GMS compared to the activated carbon reference material. To gain insights into the unique chemistry of GMS structure and composition that lead to favourable electrochemical properties, we conducted density functional theory (DFT) simulations to examine the interactions of IL with the GMS material using nanoscale, periodic models of the pristine and two different defect site-containing graphene sheets. The dominant interactions in these systems are a network of H-bonds and dispersive interactions, similar in both systems, but favouring curved graphene due to its structural complementarity with IL ions. Changes to the electron density distributions relative to those of the separate components and the superimposed effect of cations/anions and polymer matrix interactions were used as the atomic-scale measure of surface wettability.

Introduction

With the rapid advancement of our society's technological needs, a burning concern is the storage of energy. Therefore, numerous research efforts worldwide intensely focus on this challenge owing to the critical needs of portable electronics, flexible devices and hybrid/electric vehicles. Traditional capacitor systems and classical batteries have limits on the amount of energy they can store, as well as on the rate at which they can deliver that energy. To address this limitation, supercapacitors (also known as ultracapacitors) are employed due to their higher power densities, robust and long cycling, fast charging and discharging, and wide range of operating temperatures. Furthermore, they are capable of storing higher energy as compared to traditional capacitors, and they deliver energy at higher power as compared to classical batteries. More recently, R&D focus has been shifted to flexible devices due to advancements in technology and growing demands for portable, lightweight, wearable devices and adaptable electronics. In flexible capacitors, usually composite materials are used, which serve as electrodes and current collectors. The electrolyte is mostly composed of a polymer gel with good mechanical and electrical properties that separate the electrodes in order to avoid short- circuiting. Flexible capacitors are of two types: i) two-dimensional planar capacitors and ii) one-dimensional fibre-based capacitors. The present work focuses on planar capacitors that are sandwich-type, in which gel electrolytes are packaged between two identical electrodes. Nevertheless, the performance of any device highly depends upon the materials employed (electrodes and electrolytes). Metal oxides, conducting polymers, and carbon-based materials have already been thoroughly characterised[1–3]. The key

Correspondence: Amrita Jain (ajain@ippt.pan.pl)
Hirotomo Nishihara (hirotomo.nishihara.b1@tohoku.ac.jp) or
Eva Scholtzova (eva.scholtzova@savba.sk)
[1]Institute of Fundamental Technological Research, Polish Academy of Sciences, Pawińskiego 5B, 02-106, Warsaw, Poland
[2]Sapienza Università di Roma, Dipartimento di Ingegneria Meccanica e Aerospaziale, Rome 00184, Italy
Full list of author information is available at the end of the article
These authors contributed equally: Amrita Jain, Daniel Moreno-Rodríguez

properties to rank electrode materials are high specific surface area, significant porosity, good conduction properties, high stability and elevated level of electroactivity. Most carbon materials possess the aforementioned qualities; however, activated carbon, carbon nanotubes, and graphene can manifest different performances with the same electrolyte, which creates some uncertainty in their application[4,5]. For the chemical understanding of their performance ambiguity, which also affects the charge storage mechanism, and to enhance the cell's efficiency, it's important to enlist the combined potential of experimental techniques and theoretical methods, as we demonstrate hereby.

In this work, we used graphitic mesosponge (GMS), which is a custom-designed 3D carbon framework with mesoporosity as a key difference from high-quality single-layer graphene. This material has a sponge-like mesoporous structure with an average pore size of ~5.8 nm. The structure of this material lacks the stacking of graphene sheets and possesses a very high surface area of ~1940 $m^2 g^{-1}$, along with high electronic conductivity[6]. It consists of single-layer graphene walls without edge sites and features interconnected mesopores. The unique structure of GMS was expected to be advantageous for the current work compared to the microporous, commercially available activated carbon YP50F, which is used as a reference material in this study.

Along with electrodes, electrolytes also play a vital role in the performance of cells. Liquid (but not aqueous) electrolytes are the most conventional examples, which are used for supercapacitors, but clearly, they come with several shortcomings, such as a narrow potential window (1.23 V vs. standard hydrogen electrode), leakage, corrosion and safety issues. To mitigate these issues, polymer electrolytes were introduced for high-performance supercapacitors[7,8]. Among them, ionic liquid-based electrolytes (ionogels) are one of the best performing electrolytes as they can offer high ion conductivity, low vapour pressure, non-flammability, and a wide potential window[9,10]. Due to these favourable properties, ionogels are one of the potential electrolytes that can be used as a suitable power source for wearable and flexible energy storage devices. The ionogels are prepared by mixing the different ratios of host polymer and ionic liquid in a common solvent and allowing the solvent to evaporate. The resulting films have high ionic conductivity along with self-standing mechanical stability. Among a wide range of ionic liquids, 1-ethyl-3-methylimidazolium hydrogen sulphate ($[EMIM^+]HSO_4^-$) was chosen in this work, given that it is a hydrophilic ionic liquid containing sulphate ions. This IL system is also known as eco-friendly and non-corrosive, with an excellent potential window of ~3.0 V that maintains its liquid state at room temperature. Hence, to convert them into ionogels, ionic liquids must be encapsulated into a suitable polymer matrix formed by polyvinyl alcohol, as in the given case.

In the present work, we report combined electrochemical and computational investigations of different types of carbon materials as electrodes and ionogels as electrolyte material. The electrochemical characterisations show the favourable properties of GMS electrodes with ionogel electrolytes, which are rationalised by the results of nanoscale periodic models of graphene with various degrees of corrugations and the presence of defect sites. The interaction energies between the carbon electrode models and the components of the ionogel serve as measures of surface wettability as a key physical property that rationalises the experimental observations.

Experimental section

Materials and techniques used for electrode and electrolyte preparations

All the materials for this work were prepared by using two carbon materials: graphene mesosponge (GMS) and YP50F carbon (Kuraray Chemical, Japan). The preparation, characterisation and other relevant details, including the scanning microscope image of the GMS, are provided elsewhere[11]. The electrode films from these carbons were prepared by using a slurry casting method. In the process, 90 wt% of active materials (GMS and YP50F) were mixed with 10 wt% of polyvinylidene fluoride binder (PVdF) (Merck). The slurry was prepared by using a commonly employed solvent of N-methylpyrrolidone (NMP). The films were prepared on carbon cloth substrate (AVCarb, USA) and allowed to dry at 60 °C for ~8 h while NMP evaporated. The loading average mass of GMS and YP50F was ~2.2 mg and ~2.5 mg, respectively. The electrode surface area and thickness were 1 cm^2 and ~0.3 mm, respectively. An ionic liquid gel polymer (ionogel) was prepared by mixing 85 wt% of 1-ethyl-3- methylimidazolium hydrogen sulphate $EMIM^+[HSO_4]^-$ (Solvionic) with 15 wt% of polyvinyl alcohol, PVA (Merck) as a host polymer, dissolved in double-distilled water. After adequate mixing, the homogenous solution (ionic liquid and polymer) was poured into a Petri dish and allowed to evaporate at room temperature. The ionic conductivity of the prepared ionogel is 5.12×10^{-3} S cm^{-1} with nearly 0.6-0.7 mm of thickness. Upon drying, samples were stored in a desiccator. In addition to the traces of water solvent remaining in the polymer matrix, a few drops of water were introduced to increase the wettability of the electrode and electrolyte during cell assembly. Additional details of the preparation, optimisation and characterisation of the ionogels are discussed in our previous work[12].

Cell preparation and electrochemical testing

Two symmetric supercapacitor cells were prepared by directly sandwiching the ionogel film between either the

GMS or the YP50F carbon electrodes using the Swagelok cell. The free-standing ionogel film is practically a solid with ionic liquid trapped in its polymer matrix owing to its continuous three-dimensional network of PVA scaffold. The cell can be described as a 3-component system, such as GMS | Ionogel | GMS (Cell A) and YP50F | Ionogel | YP50F (Cell B). The role of the ionic liquid is multifaceted, given that it contributes to the ionic conductivity of the host polymer (PVA in the present case) and also increases the plasticity of the host polymer. Similarly, PVA's hydrophilic functional groups lower bulk resistance and stabilise the interfacial contact with the electrode[13] (see also the H-bonding network from the computational results below). The cells for the present studies were prepared under a fume hood, and after preparation, the cells were allowed to rest for ~1-2 hours.

The electrochemical characteristics of Cells A and B were examined by using cyclic voltammetry (CV), electrochemical impedance spectroscopy (EIS), and galvanostatic charge-discharge (GCD) testing at room temperature and under ambient conditions using a Bio-Logic VMP3 electrochemical workstation. CV measurements were recorded at varied scan rates from 1 mV s^{-1} to 100 mV s^{-1} in the potential range from 0 V to 2.0 V. The EIS measurements were carried out in the frequency range from 1 mHz to 200 kHz with a signal range of 10 mV. The GCD measurements were conducted at various current densities from 0.1 to 0.5 mA cm^{-2} between the voltages from 0 to 1.0 V. The internal resistance (IR) was calculated for each cell by recording the sudden voltage drop in the discharge branch (ΔV) using the formula IR: ΔV/2i, where i represents the applied constant current[14]. The formulas used to calculate the specific capacitance values of a single electrode from electrochemical impedance spectroscopy and galvanostatic charge-discharge technique are provided in Supplementary Information (see Equations S1-S2).

Computational methodology

For the nanoscale periodic models, the density functional (DFT) method in the Vienna ab initio simulation package (VASP)[15,16] was employed to optimise structural models in order to provide atomic level description for the most dominant networks of interactions acting in the supercapacitor cells. Blochl's projector augmented wave (PAW) technique[17,18] was used to describe the electron–ion interactions. The exchange-correlation energy was defined as a generalised gradient approximation (GGA) using the functional proposed by Perdew, Burke and Ernzerhof (PBE)[19] together with the DFT-D3 scheme for corrections of dispersion forces[20].

Owing to the large computational cells, the Brillouin-zone sampling was restricted to the Γ point[21,22]. Furthermore, the electron density difference ($\Delta\rho^e$) was calculated from the optimised periodic structure and its separate, unrelaxed components to investigate how the electron density (ρ^e) was distributed among atoms and what type of interactions were formed. While these simulations employ stationary DFT calculations, the optimised structures and interaction energetics provide insights into the equilibrium properties of the system, such as surface wettability and interfacial interactions, which are key determinants of the electrochemical performance observed experimentally.

The structural models for simulations were prepared closely following the experimental data. The model of pristine graphene (G) was supplemented with a model of the modified graphene sheet (MG) by a Stone-Wales defect (SW) at its centre. MG contained two seven-membered rings and two five-membered-rings[23]. Both these structures were intercalated by the mixture of 85 wt% of ionic liquid, $[EMIM]^+$ HSO_4^-, and 15 wt% of PVA polymer, modelled by pentamer unit, $H[CH_2CH(OH)]_5$-H (P). The computational cell *8a8bc* was built by a graphene unit cell with the lattice parameters $a = 2.468$ Å, $b = 2.468$ Å and $\alpha = \beta = 90°$, $\gamma = 120°$, while the c value was increased to allow enough space (25 Å) to contain one PVA molecule, six pairs of $[EMIM]^+$ and HSO_4^- ions. Two models studied in the present work were labelled as G-P-IL and MG-P-IL. Additionally, to isolate the influence of graphene defect chemistry on ionic liquid adsorption, a third model was also constructed for protonated-vacancy graphene (VG-IL). Each of the G, MG, and VG models interacted with six $[EMIM]^+$ cations and six HSO_4^- anions on the same face of the models, hence, enabling direct comparison of defect-driven wettability and charge redistribution effects.

Results and discussion

Toward the goal of comparing and contrasting the mechanism of interfacial charge transfer processes between electrode and electrolyte, and to understand the differences in electrochemical performance of different types of carbon materials with the same ionogel electrolyte, the electrochemical evaluation of Cells A and B was carried out first. The experimental observations were further substantiated by theoretical modelling of the network of interfacial interactions.

Experimental observations

Figure 1 shows the results of CV measurements performed with the two supercapacitor cells. In order to determine the voltage stability of the cells as a function of the carbon electrodes, the CV curves were recorded under the potential range from 0 V to 2.0 V at a scan rate of 5 mV s^{-1}. The corrosion current above 1.5 V is lower in Cell A with GMS than in Cell B with YP50F electrodes. This difference can be rationalised by the presence or

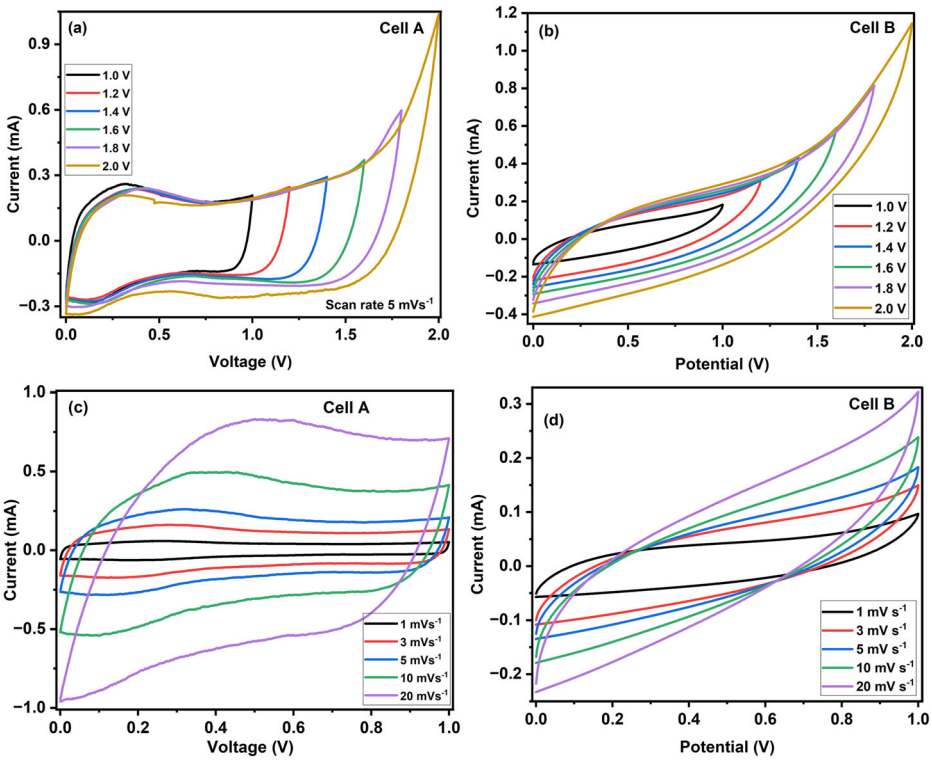

Fig. 1 Cyclic voltammetry (CV) studies of supercapacitor cells. Comparative CV curves of Cells A and B with GMS and YP50F carbon electrodes and ionogel electrolytes form $[EMIM]^+HSO_4^-$ ionic liquid and PVA polymer matrix mixture at various voltages with fixed scan rate of 5 mV s^{-1} between 0 and 2.0 V (**a**, **b** and different scan rates of 1, 3, 5, 10, 20 mV s^{-1} and in the potential range from 0 V to 1.0 V (**c**, **d**).

absence of edge sites[6]. In the case of Cell A, corrosion processes can more readily take place than on the open face of the material. We anticipate that the presence of corrosion current would be lower and the cell stability would increase by minimising the water content of the ionogel, which can, in turn, be prohibitive for cell fabrication. The choice of the 85:15 ($[EMIM]^+HSO_4^-$:PVA) composition was based on our previous systematic investigation[12], where we evaluated the structural and thermal properties of ionogels at different ratios. Differential scanning calorimetry (DSC) and thermogravimetric analysis (TGA) confirmed that the 85:15 films exhibited (i) a higher glass transition temperature ($T_g = 43$ °C) compared to other compositions (ratios) of $[EMIM]^+HSO_4^-$:PVA, (ii) a distinct low-temperature endothermic region associated with residual water loss, and (iii) a stable thermal profile until the onset of pyrolysis above 280 °C. These findings indicate that most of the free water was removed, and only tightly bound water remained in the polymer-ionic liquid matrix, which directly contributes to reduced corrosion current and improved cell stability.

The CV profile of Cell B in Fig. 1 is significantly distorted from the ideal rectangular shape, which indicates a large internal resistance. In contrast, the CV shape in Cell A is less distorted due to its higher electrical conductivity. The butterfly shape of the CV profiles in Fig. 1c for Cell A is maintained even up to 20 mV s^{-1}, which shows that the cell has lower resistance even at higher voltages, as an advantageous property for the GMS materials. The CV curves in Fig. 1d with upward slopes for Cell B revealed the typical behaviour when the internal resistance of a supercapacitor is significantly high. In Cell B, the capacitance is quite small (~47.9 F g^{-1}), as can be seen from the CV curve (Fig. 1b). This can be attributed to the poor wettability of the ionogel electrolyte due to the microporous structure of YP50F. In contrast, GMS shows larger capacitance (~76.6 F g^{-1}), indicating much better wettability of the framework due to its interconnected mesoporous structure, where the electrolyte ionogel can fill its pores with ions. The higher resistance of Cell B is due to the difference in electric conductivities of GMS and YP50F, with the former being significantly better (~8 S cm^{-1}) in comparison to the latter (~2 S cm^{-1})[6].

The supercapacitor Cells A and B have also been evaluated by using the EIS technique in the frequency range from 1 mHz to 200 kHz as shown in Fig. 2a. For an ideal supercapacitor, the EIS plot displays two significant parts: a curved line with a maximum value in the high frequency region (at low Z' values) followed by a straight vertical line which parallels the coordinate axis (Y-axis) in the lower

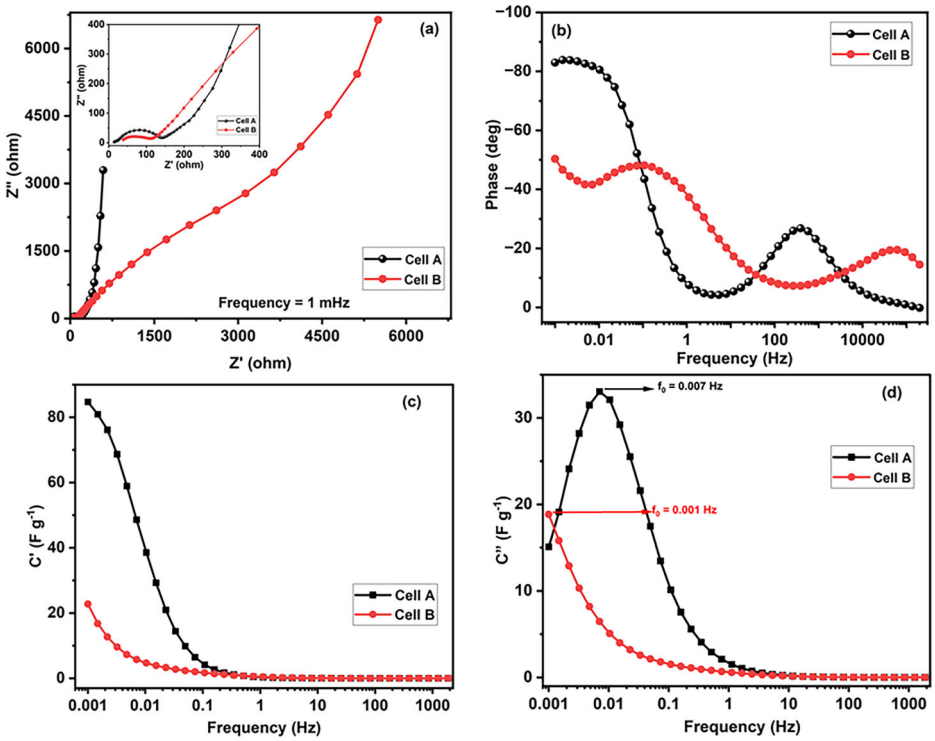

Fig. 2 Electrochemical impedance spectra (EIS) of supercapacitor cells. EIS plots (**a**) of Cells A (GMS/$[EMIM]^+HSO_4^-$:PVA) and B (YP50F/$[EMIM]^+HSO_4^-$:PVA) with inset shows the expanded view of high frequency region (Z′ is defined a real impedance), **b** Variation of phase angle with respect to frequency, Bode plots; variation of (**c**) real capacitance (C′) and **d** imaginary capacitance (C″) with respect to frequency.

frequency region (at high Z' values). The EIS plots of Cells A and B show markedly different patterns in the expanded view of the high-frequency region (inset), which indicate significant differences in the bulk resistance (R_b) and charge transfer resistance (Rct). The Rb values are related to the resistance of the electrode and electrolyte, which simplifies, in our case, the difference in the electrode materials, GMS and YP50F, since the current collector and electrolyte are the same materials. The Rb values of Cells A and B were found to be nearly 12.9 and 38.6 Ω, respectively. Furthermore, Rct generally arises from the Faradic charge process at the electrode/electrolyte interface, where redox processes can be influenced by the presence of impurities or undesirable side-reactions occurring at the surface of the electrode. However, in the case of electric double layer capacitors (EDLCs), no significant redox reaction can take place; thus, the origin of the high frequency profile in EIS has not been fully understood yet. For example, Liu et al.[24] have conducted systematic studies on the relationship between pore dimension and Rct. They found that the value of Rct increases with the increase in the interface between the carbon electrode and the electrolyte used. In Fig. 2a, Cell B shows a much smaller Rct (72.1 Ω) than Cell A (123.29 Ω). It has been reported that R_{ct} increases with the increase of carbon/electrolyte contact area using model membrane electrodes with ordered cylindrical nanopores. Thus, the larger R_{ct} in Cell A suggests that the GMS nanopores with larger sizes than YP50F are more wetted by the ionogel electrolyte[24]. Given Cell B's low capacitance and large internal resistance, as indicated by the impedance plot in Fig. 1a, we can anticipate less sufficient pore wetting with the electrolyte in YP50F[25] than with ion GMS. Also, higher R_{ct} in Cell A suggests that the developed mesopores of GMS-based electrodes are saturated by ionogel electrolytes more easily compared to YP50F. Moreover, the single electrode specific capacitance was calculated by using Equation S1 with data from Fig. 1c, d to be of the order of ~88 and 38 F g^{-1}, respectively, for Cells A and B.

Figure S1 presents the EIS results together with the equivalent circuit modelling. The experimental data for both the cells (black dots) were fitted using the equivalent circuit shown in panel (c), where the red lines represent the simulated response. As can be seen from Fig. S1a, Cell A exhibits a depressed semicircle in the high-frequency region, followed by a diffusion tail at low frequencies. The fitted parameters reveal resistive contributions of R2 = 21.75 Ω, R1 = 113.1 Ω, and R3 = 1121 Ω. Despite the presence of interfacial resistance, the Warburg

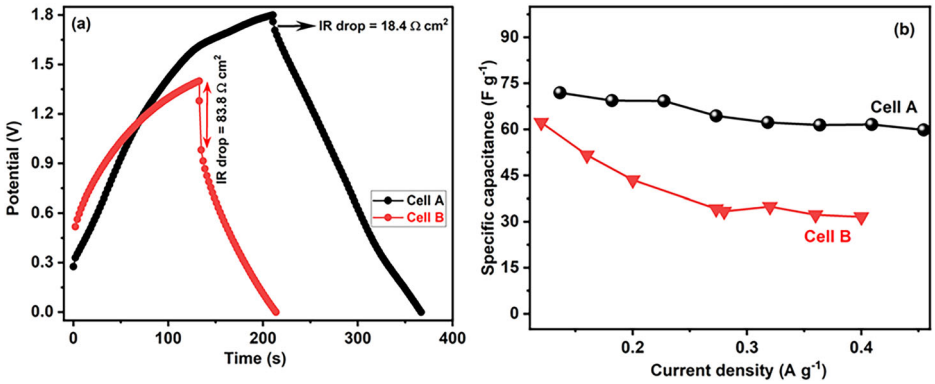

Fig. 3 Galvanostatic charge-discharge curves of supercapacitor cells. a Galvanostatic charge-discharge profiles of Cell A (up to 1.8 V) and Cell B (up to 1.4 V) at a current density of 0.2 A g^{-1}, **b** variation of specific capacitance for Cells A and B with respect to current densities.

element values (W1-R = 66.25, W1-T = 3.87, W1-P = 0.52) suggest relatively moderate diffusion limitations, indicating that ion transport within the GMS electrode is still facilitated to a reasonable extent. The constant phase element exponent (CPE2-P = 0.50) reflects a degree of surface heterogeneity but also points to stable interfacial charge storage behaviour. On the other hand, as can be seen from Fig. S1b, Cell B exhibits a smaller semicircle at high frequency and a nearly vertical low-frequency line. The fitted resistances are R1 = 25.96 Ω, R2 = 88.57 Ω, and R3 = 1320 Ω, with a larger contribution from interfacial resistance compared to Cell A. Although the capacitive response is closer to ideal (CPE2-P = 0.81), the Warburg parameters (W1-R = 17752, W1-T = 728.5, W1-P = 0.56) reveal substantial diffusion constraints, suggesting that ion transport within the porous YP50F electrode is strongly hindered despite its high surface area. Cell A demonstrates a more balanced impedance profile, with manageable diffusion resistance and stable charge-transfer properties. These results suggest that the GMS-based Cell A, when combined with the $[EMIM]^+H$-SO_4^-:PVA ionogel electrolyte, provides superior interfacial compatibility and more efficient ion transport compared to the YP50F-based Cell B. These results confirm the facile transport of electrolyte ions $[EMIM]^+$ and $[HSO_4]^-$ in the GMS carbon frame in line with the CV results and GCD (see below).

Figure 2b shows the variation of phase angle with respect to frequency for Cells A and B with the expectation of a phase angle of 90 ° for the full frequency region[26] in an ideal supercapacitor cell. In our case, in the lower frequency region (<1 Hz), Cells A and B have phase angles of ~83° and ~50°, respectively, which clearly confirms the superior capacitive behaviour of Cell A with the GMS electrode. To further investigate and understand the ion diffusion kinetics, the real (C') and imaginary (C") capacitance values were plotted with respect to frequency, as shown in Fig. 2c, d. The values at low frequency (<1 Hz) refer to the real capacitance of the cells with a close agreement to those calculated from galvanostatic charge-discharge measurements (see below). Furthermore, the slopes of the curves at higher frequencies are almost zero, which means the cells are not capacitive. However, this is typical behaviour for supercapacitors in this frequency region. Clearly, the real capacitance values C' of Cell A are higher than those of Cell B, which again confirms the better wettability of GMS as an electrode with the ionogels.

The variation of imaginary capacitance (C") with respect to frequency for Cells A and B is shown in Fig. 2d. The C" values can be used as a representation of the energy dissipated through the non-reversible ion transport process involving the rotational and translational motions of ions inside the electrolyte material. The maximum of C" versus frequency curve marks the relaxation frequency f_0. In our case, Cells A and B have f_0 = 7 mHz and 1 mHz, respectively. A comparatively higher value of relaxation frequency in the case of Cell A indicates that in the GMS electrode framework, the electrolyte ions have more space to move in the mesopores, which can lead to enhanced electrolyte mobility.

Lastly, galvanostatic charge-discharge (GCD) assessments were performed to calculate the parameters, such as specific capacitance and internal resistance. The comparative GCD curves for Cells A and B are provided in Fig. 3a. The galvanostatic cycling test shows the enhanced stability of the GMS material as the cell comfortably reached up to 1.8 V at a current density of 0.2 A g^{-1} with negligible internal resistance (IR) compared to YP50F, with a high resistance that was only stable up to 1.4 V. The IR values calculated for Cells A and B were found to be ~18.4 and 83.8 Ω cm^2, respectively. The lower IR value for Cell A proves the compatibility of GMS carbon with the optimised ionogel and the favourable electrode-electrolyte interaction at the interface of the cell. This also rationalises the different corrosion behaviours in

GMS and YP50F. These electrochemical features can be attributed to their differing amount of edge sites, as lower edge sites of GMS contribute to potentially wider potential windows and enhanced stability towards the electrolyte well. GCD results are also aligned with EIS and CV, and the same trend is reflected for the specific capacitance values (single electrode capacitance calculated from Equation S2) as well, with values of ~72 and 62 $F g^{-1}$, respectively, despite a smaller difference in the specific capacitance values than the internal resistance values.

The variation of specific capacitance with respect to current densities (Fig. 3b) shows that with an increase in the current density, the capacitance of Cell B decreases more rapidly than Cell A, confirming that Cell A has a favourable rate of maintaining cell capacity. The different rates of decrease in the capacitance values can be explained based on atomic-level structure features related to the movement of ions in the electrode and electrolyte. When the current density is low, the electrolyte ions have enough time to diffuse through the pores of electrodes (at a higher rate in GMS than in YP50F), where even the small pores are accessible to the ions, resulting in high capacitance. However, at high current densities, the movement of ions is too fast to explore all the micropores in the material. In turn, the diffusion of ions occurs on a limited path inside the pores of the electrodes, thereby decreasing the capacitance values. In the case of Cell A, the capacitance is decreasing only gradually, which confirms the suitability of combining $[EMIM]^+HSO_4^-$:PVA ionogel electrolyte with GMS electrodes for technologically viable supercapacitor architectures.

Overall, the electrochemical measurements confirmed that Cell A shows superior electrochemical performance in terms of capacitance, stability towards electrodes and excellent wettability with respect to the commercial carbon-based (YP50F) electrode. We hypothesise that this is due to a lower amount of edge sites of GMS as well as its favourable curvature corresponding to its mesopores, which contributes to the enhanced performance of templated carbons over amorphous activated carbons. Guided by our experimental results, we turned to computational modelling to unravel the atomic-scale interplay between the electrode and electrolyte, thereby shedding light on the key compositional and structural factors behind the GMS system's enhanced performance. Considering the experimental challenges in elucidating the surface structure of electrodes incorporating ionogels, theoretical calculations were performed to provide molecular- and atomic-level insights into the GMS and YP50F electrodes as well as the ionogel–electrode interface.

Computational modelling

The atomic-scale explanations for the differences between Cells A and B with mesoporous and microporous carbon materials in the absence and presence of carbon edge sites prompted us to conduct material structure modelling using periodic boundary conditions to further substantiate the rationale of experimental data.

The optimised periodic models revealed that the planes of graphene sheets became spontaneously corrugated in response to the electrode interactions with the intercalated electrolyte ions and molecules. The C atoms in the sheet presented about 1 Å deviations along the perpendicular direction to the basal planes for both G-P-IL and MG-P-IL models with pristine (G) and modified (MG) graphene surfaces relative to their co-planar starting atomic positions. The optimised *d*001 values of 11.2 and 11.7 Å were similar for both models within 0.5 Å. In the interlayer space, the PVA pentamer, P, and $[EMIM]^+$ HSO_4^- ions were arranged in a bilayer fashion as dictated by the length of the $[EMIM]^+$ cations. In some cases, the cations displayed a perpendicular arrangement with respect to the graphene sheet (Fig. 4) upon structural optimisation. In the upper part of the bilayer, as shown in Fig. 4, the $[EMIM]^+$ cations interact similarly with the graphene sheet in both models. Likewise, the HSO_4^- anions interacted with the graphene sheet in the G-P-IL model similarly to the MG-P-IL, as can be numerically followed by Table S1. In the lower part of the bilayer from Fig. 4, the PVA polymer presented an expanded chain-like arrangement with respect to the graphene sheet, as its alcohol –OH functional groups and the aliphatic –CH2– groups form H-bonding and dispersion interactions with the aromatic π-system. The PVA polymer with the $[EMIM]^+$ and HSO_4^- ions interacted similarly in both models (Table S1-2), with a minor difference in which polymer matrix model PVA had two –OH groups pointed toward the pristine graphene surface in the G-P-IL model while only one –OH group in MG-P-IL model with more $-CH_2^-$ groups interacting more with the modified graphene sheet.

Table S1 quantitatively describes the network of H-bonding interaction patterns as the common weak interactions among the C surface, cations, anions, and polymer matrix mimic. The range of H-bonds is notable from weak (2.5 to 3.0 Å) to strong (<2.0 Å) H···acceptor atom distances (Table S1). Most strikingly, in the G-P-IL model, the $[EMIM]^+$ cations form CH···O hydrogen bonds with the HSO_4^- anions with a median distance of 2.53 Å, while in MG-P-IL models, this was a much shorter 2.02 Å (Table S2). The significant 0.5 Å shortening of the CH···O hydrogen bonds is due to the rearrangement of the ions in the vicinity of the defect site. Moreover, the $[EMIM]^+$ units formed weaker CH···O hydrogen bonds with the P molecule, with a median of 2.76 Å in models of Fig. 4. A similar situation was found for the CH···O H-bonds formed among the PVA and the HSO_4^- anions, which formed strong OH···O H-bonds with median values of

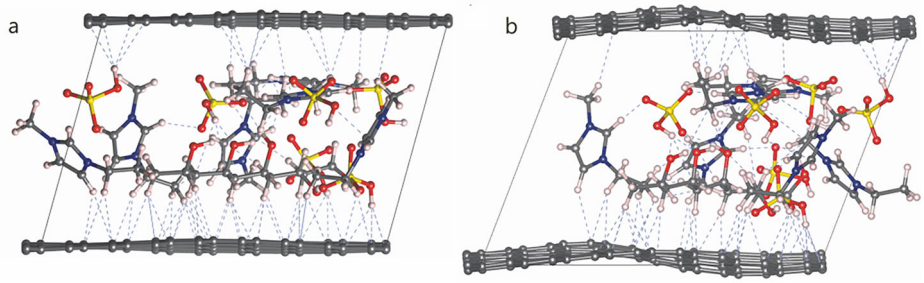

Fig. 4 Optimised structures of G-P-IL and MG-P-IL models. Optimised structures of G-P-IL model (**a**) and MG-P-IL model (**b**). The atoms are represented in grey (C atoms), white (H atoms), blue (N atoms), red (O atoms) and yellow (S atoms). The H-bonds are represented by the blue dashed lines.

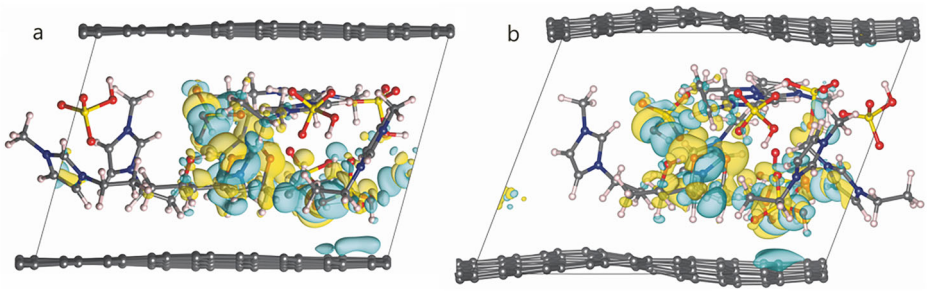

Fig. 5 Electron density difference between PVA pentamer and surrounding system. Electron density difference plot between the PVA pentamer (P) and the rest of the system ($[EMIM]^+$ HSO_4^- and the graphene sheets) in G-P-IL (**a**) and MG-P-IL (**b**) models. The blue colour represents electron depletion, and the yellow represents electron accumulation. The iso-surface contour level is 0.0008 e $Å^{-3}$.

1.69 and 1.73 Å in G-P-IL and MG-P-IL, respectively. On the other hand, the main form of electrolyte/electrode interaction was a network of weak interactions that was stronger with the HSO_4^- ions due to the acidity of the proton, forming OH···π interactions with medians of 2.54 in G-P-IL and 2.56 Å in MG-P-IL. This is to be compared to the interactions of the $[EMIM]^+$ ion and PVA molecule through the CH···π interactions with median values of 2.84 Å and 2.90 Å for the G-P-IL structure. Peculiarly, in the MG-P-IL structure, these values were reversed as the $[EMIM]^+$ cations formed weaker (2.90 Å), the PVA polymer formed stronger (2.83 Å) interactions as a result of the compromised π-electron cloud due to the presence of mixed ring sizes.

Another way to visualise the global impact of electrolyte and electrode interactions is to consider electron density difference ($\Delta\rho^e$) plots. Figure 5 reveals the predominant electrostatic contribution of the H-bond network associated with the PVA unit. The majority of the density perturbations involve the $[EMIM]^+$ and HSO_4^- ions surrounding the PVA unit, with a smaller contribution as the PVA unit touches the π-electron cloud in the bottom right corner. The alternating appearance of positive (decreased ρ^e) and negative (increased ρ^e) regions suggests significant polarisation of the electron cloud; thus, the importance of induced charge/dipole interactions. In contrast, the graphene sheets exhibit only a modest interaction with the PVA polymer mimic. This was expected from Table S1 as the separation between PVA and G/MG surface was the longest among all. However, when taken all together, the dissociation energy (ΔE^{QM}) of the PVA polymer mimic remains identical within 2 kJ mol^{-1} for G-P-IL (312 kJ mol^{-1}) and MG-P-IL (310 kJ mol^{-1}) as calculated from the equation $\Delta E^{QM} = E^{QM}([EMIM]^+HSO_4^-\text{-G/MG}) + E^{QM}(\text{PVA}) - E^{QM}(\text{PVA-}[EMIM]^+ HSO_4^-\text{-G/MG})$. These indicate that the presence of PVA will have a similar impact on the stability of the ionogel versus the wettability of the electrode surface due to the different network of intermolecular interactions (Table S1). Supporting information (Fig. S2) shows additional electron density difference plots with reduced iso-surface level in order to visualise the changes in the π-electron cloud corresponding to the electrolyte components. It is remarkable to recognise that electron density variations show a correlation with the curvature of the graphene sheets. Specifically, the sheets became downwardly curved in the region of increased electron density and vice versa for the upwardly curved domain.

The IL adsorption models G-IL, MG-IL, and VG-IL revealed distinct H-bonding patterns between the

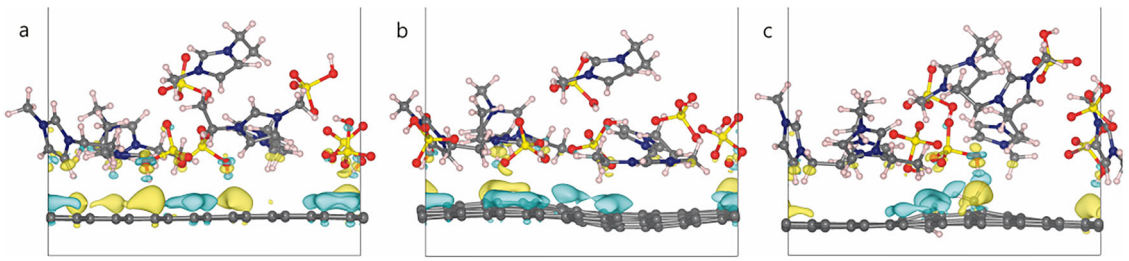

Fig. 6 Electron density difference between ionic liquid and graphene sheets. Electron density difference plots between ionic liquid ($[EMIM]^+HSO_4^-$) and graphene sheets for (**a**) pristine G-IL, **b** Stone-Wales defect containing MG-IL, and **c** VG-IL with protonated-vacancy site. Blue regions ($\Delta\rho < 0$) indicate electron depletion, yellow regions ($\Delta\rho > 0$) show electron accumulation. Isosurface contour level is 0.001 e/Å^3.

$[EMIM]^+$ and HSO_4^- ions and graphene surfaces (Fig. 6 and Fig. S3). The HSO_4^- anion and $[EMIM]^+$ cation exhibit distinct, defect-sensitive adsorption behaviours across graphene models (G-IL, MG-IL, VG-IL), with implications for the electrochemical performance. HSO_4^- shows progressively stronger O-H···π interactions with increasing defect severity from pristine graphene (median 2.54 Å) to shorter (median 2.48 Å) at SW defects and localised at protonated vacancies (median 2.49 Å). While pristine graphene offers a uniform π-electron cloud that supports electrostatic interactions, SW defects disrupt this delocalisation and impose steric hindrance that can slightly reduce HSO_4^- anions interaction efficiency of HSO_4^- anions. In contrast, protonated vacancies provide strong localised binding, but restrict the locus of adsorption sites by concentrating H-bonding at the defect site. $[EMIM]^+$ cations consistently form weaker C-H···π/C interactions (median 2.65–2.78 Å), yet their adsorption density varies with surface topology. In the G-IL model, they adopt a tilted orientation forming weak interactions (median 2.76 Å), while MG-IL's SW curvature promotes stronger interactions (median 2.69 Å) via favourable planar orientation and enhanced surface contact. VG-IL, however, shows reduced cation adsorption, as protonated vacancies repel cations from the defect core, forcing interactions with adjacent aromatic rings instead.

Together, these trends highlight the defect-dependent interplay between anion and cation binding: the SW defect in MG-IL optimally enhances both HSO_4^- interactions (shortened by 0.07 Å vs. G-IL) and cation density, correlating with its superior capacitance. Conversely, VG-IL's localised but sparse bonding, stronger for anions and weaker for cations, accounted for its higher resistance and limited ion mobility.

Electron density difference analysis confirmed that defect-induced charge redistribution governs IL adsorption and electrochemical behaviour. In G-IL, symmetric electron density accumulates over the π-system (Fig. 6a) and depletion near $[EMIM]^+$ ions' alkyl chains supports weak, delocalised C-H···π interactions, with cations adopting a tilted orientation. HSO_4^- displayed weak O-H···π interactions (median 2.54 Å) and mild charge accumulation near its oxygens, reflecting low but uniform interfacial polarisation.

MG-IL exhibited stronger, localised polarisation at the SW defect (Fig. 6b), enhancing $[EMIM]^+$ adsorption via increased curvature and contact area, favouring a near-planar orientation. HSO_4^- also showed intensified charge accumulation near defect edges and formed shorter O-H···C bonds (median 2.49 Å). This dual enhancement boosts ionic binding, but slightly disrupts long-range ordering, which may moderate wettability.

VG-IL features the most localised hotspots (Fig. 6c) at protonated vacancies, enabling short O- H···C hydrogen bonds with HSO_4^-. However, $EMIM^+$ shows asymmetric charge depletion along its alkyl chains, which orient toward the vacancy, limiting adsorption to the surrounding rings. This spatial confinement led to sparse ion coverage and restricted mobility.

Collectively, these results establish a defect-dependent hierarchy of interfacial behaviour. VG- IL offers the strongest localised interactions but poor coverage, MG-IL achieves a balanced state of enhanced yet accessible binding sites, and G-IL provides uniform but weaker interactions. The electronic polarisation trends directly correlate with electrochemical features; MG-IL's moderate charge localisation and high interaction density explain its superior capacitance, while VG-IL's concentrated binding sites limit performance due to ion transport bottlenecks. This trend is further supported by adsorption energies of the six pairs of $[EMIM]^+$ and HSO_4^- ions and the carbon material models, which follow the order MG-IL (–314 kJ mol^{-1}) > G-IL (–299 kJ mol^{-1}) » VG-IL (–226 kJ mol^{-1}), confirming that SW defects enhance interfacial stability, while protonated vacancies, despite strong local binding, reduce overall energetic favourability due to limited adsorption coverage.

Conclusions

From a comparative analysis of a novel carbon material, GMS, and activated carbon, YP50F, as electrodes and

ionogel electrolyte with $[EMIM]^+$ and $(HSO_4)^-$ ions, PVA polymer matrix, we measured favourable electrochemical properties for the templated carbon material GMS from parallel cyclic voltammetry, electrochemical impedance spectroscopy, and galvanostatic charge discharge. These superior electrochemical features of GMS can be attributed to their differing amount of edge sites, as lower edge sites contribute to potentially wider potential windows and enhanced stability towards the electrolyte well. At the atomistic level, dispersion corrected DFT simulations revealed that interaction with the ionogel components induced spontaneous corrugation of the graphene sheets, especially when the Stone-Waals defect is present, mimicking GMS's structural curvature and promoting ion accessibility. Thus, SW defect-containing models (MG) enhance local ionic density and contact area that can support improved adsorption of $[EMIM]^+$ and $(HSO_4)^-$ ions compared to pristine (G) or vacancy-defected systems (VG). Although pristine graphene formed interactions with PVA molecule and IL ions, the moderate curvature in MG enabled a more favourable spatial arrangement for ion accumulation, striking a balance between interaction strength and surface coverage. Further, electron density difference plots confirmed that the key interfacial interactions involved electrostatic polarisation driven by H-bonding interaction involving the π-cloud, and modulated by defect topology. Overall, the findings highlight that optimal electrochemical behaviour arises not simply from maximising binding energies, but from achieving a geometrically and electronically favourable interface that supports rapid, reversible ion transport. These insights underscore the critical role of pore architecture, defect chemistry, and electrolyte design in advancing flexible, high-voltage energy storage devices, positioning GMS-type materials as a promising platform for next-generation supercapacitors.

Acknowledgements
E.S. received financial support from the Slovak Academy of Sciences, Slovakia (V4- Japan/JRP/2021/96/AtomDeC) through the research project cooperation in the AtomDeC Consortium within the 2nd Joint Call on "Advanced Materials" and by the Scientific Grant Agency VEGA (Grant, 2/0026/23). A.J. received financial support from the National Centre for Research and Development (NCBR, Poland); Project number: V4-Japan/2/17/AtomDeC/2022. Part of the Research results was obtained using the computational resources procured in the national project National Competence Centre for High Performance Computing (project code: 311070AKF2), funded by the European Regional Development Fund, EU Structural Funds, Informatization of society, Operational Programme Integrated Infrastructure. M.M. acknowledges the Ministry of Education, Youth and Sports, Czech Republic (contract no. 8F21007) under the Visegrad Group-Japan 2021 Joint Call on "Advanced Materials" in cooperation with the International Visegrad Fund.

Author details
[1]Institute of Fundamental Technological Research, Polish Academy of Sciences, Pawińskiego 5B, 02-106, Warsaw, Poland. [2]Sapienza Università di Roma, Dipartimento di Ingegneria Meccanica e Aerospaziale, Rome 00184, Italy. [3]Advanced Institute for Materials Research (AIMR-WPI)/Institute of Multidisciplinary Research for Advanced Materials, Tohoku University, 2-1-1 Katahira, Aoba-ku, Sendai 980-8577, Japan. [4]Department of Chemistry, The University of British Columbia, Okanagan, Kelowna, BC V1V 7V1, Canada. [5]Department of Chemistry and Physico-Chemical Processes, Faculty of Materials Science and Technology, VSB-Technical University of Ostrava, 17. listopadu 2172/15, 708 00, Ostrava-Poruba, Czech Republic. [6]Institute of Inorganic Chemistry, Slovak Academy of Sciences, Dúbravská cesta 9, 845 36, Bratislava, Slovakia

Author contributions
A.J. performed all experiments and conceived the experimental concept of this work. D.M.R. carried out the simulations with the guidance of E.S. and R.S. S.I. assisted in electrochemical analysis. M.M. assisted in methodology. H.N. contributed to experimental guidance and funding acquisition. All authors contributed to writing, reviewing, and editing of the work and finalising the manuscript.

Conflict of interest
The authors declare that they have no known competing financial interests or personal relationships that could have influenced the work reported in this paper.

Ethics declaration and consent to participate
Ethics approval and consent to participate were not required for this study because it did not involve human participants or experiments on live vertebrates. All methods were performed in accordance with relevant guidelines and regulations.

Publisher's note
Springer Nature remains neutral with regard to jurisdictional claims in published maps and institutional affiliations.

Supplementary information The online version contains supplementary material available at https://doi.org/10.1038/s41427-026-00644-9.

Received: 27 June 2025 Revised: 17 December 2025 Accepted: 4 March 2026
Published online: 01 April 2026

References
1. Reenu, S. O., Phor, L., Kumar, A. & Chahal, S. Electrode materials for supercapacitors: a comprehensive review of advancements and performance. *J. Energy Storage* **84**, 110698 (2024).
2. Tundwal, A. et al. Developments in conducting polymer-, metal oxide-, and carbon nanotube-based composite electrode materials for supercapacitors: a review. *RSC Adv.* **14**, 9406–9439 (2024).
3. Alam, S. et al. Recent progress in polypyrrole and its composites with carbon, metal oxides, sulfides and other conducting polymers as an emerging electrode material for asymmetric supercapacitors. *J. Energy Storage* **85**, 110955 (2024).
4. Ahmad, H., Khan, R. A., Koo, B. H. & Alsalme, A. Systematic study of physicochemical and electrochemical properties of carbon nanomaterials. *RSC Adv.* **12**, 15593–15600 (2022).
5. Largeot, C. et al. Relation between the ion size and pore size for an electric double-layer capacitor. *J. Am. Chem. Soc.* **130**, 2730–2731 (2008).
6. Nishihara, H. et al. Oxidation-resistant and elastic mesoporous carbon with single-layer graphene walls. *Adv. Funct. Mater.* **26**, 6418–6427 (2016).
7. Samantaray, S., Mohanty, D., Hung, I.-M., Moniruzzaman, M. & Satpathy, S. K. Unleashing recent electrolyte materials for next-generation supercapacitor applications: a comprehensive review. *J. Energy Storage* **72**, 108352 (2023).
8. Singh, S., Zhang, Y., Hashmi, S. A. & Yang, F. Supercapacitors with cotton shell-derived activated carbons and porous polymer electrolyte films. *RSC Adv.* **15**, 9787–9800 (2025).
9. Jamil, R. & Silvester, D. S. Ionic liquid gel polymer electrolytes for flexible supercapacitors: challenges and prospects. *Curr. Opin. Electrochem* **35**, 101046 (2022).
10. Liu, X. et al. Aligned ionogel electrolytes for high-temperature supercapacitors. *Adv. Sci.* **6**, 1801337 (2019).
11. Nagy, P. B. et al. Insight into the structural changes upon ultrasonic fragmentation and dispersion of carbon nanomaterials of different dimensions and bulk moduli. *Carbon* **244**, 120616 (2025).

12. Pietrzyk-Thel, P. et al. Flexible, tough and high-performing ionogels for supercapacitor application. *J. Materiomics* **11**, 100833 (2025).
13. Alipoori, S., Mazinani, S., Aboutalebi, S. H. & Sharif, F. Review of PVA-based gel polymer electrolytes in flexible solid-state supercapacitors: opportunities and challenges. *J. Energy Storage* **27**, 101072 (2020).
14. Hatzell, K. B. et al. A high performance pseudocapacitive suspension electrode for the electrochemical flow capacitor. *Electrochim. Acta* **111**, 888–897 (2013).
15. Kresse, G. & Hafner, J. Ab initio molecular dynamics for open-shell transition metals. *Phys. Rev. B* **48**, 13115–13118 (1993).
16. Kresse, G. & Furthmüller, J. Efficiency of ab-initio total energy calculations for metals and semiconductors using a plane-wave basis set. *Comput. Mater. Sci.* **6**, 15–50 (1996).
17. Blöchl, P. E. Projector augmented-wave method. *Phys. Rev. B* **50**, 17953–17979 (1994).
18. Kresse, G. & Joubert, D. From ultrasoft pseudopotentials to the projector augmented-wave method. *Phys. Rev. B* **59**, 1758–1775 (1999).
19. Perdew, J. P., Burke, K. & Ernzerhof, M. Generalized gradient approximation made simple. *Phys. Rev. Lett.* **77**, 3865–3868 (1996).
20. Grimme, S., Antony, J., Ehrlich, S. & Krieg, H. A consistent and accurate ab initio parametrization of density functional dispersion correction (DFT-D) for the 94 elements H-Pu. *J. Chem. Phys.* **132**, 154104 (2010).
21. Monkhorst, H. J. & Pack, J. D. Special points for Brillouin-zone integrations. *Phys. Rev. B* **13**, 5188–5192 (1976).
22. Kratzer, P. & Neugebauer, J. The basics of electronic structure theory for periodic systems. *Front. Chem.* **7**, 106 (2019).
23. Tian, W., Li, W., Yu, W. & Liu, X. A review on lattice defects in graphene: types, generation, effects and regulation. *Micromachines* **8**, 163 (2017).
24. Liu, H. et al. Nanoporous membrane electrodes with an ordered array of hollow giant carbon nanotubes. *Adv. Funct. Mater.* **33**, https://doi.org/10.1002/adfm.202303730 (2023).
25. Mohit, Yadav, N. & Hashmi, S. A. High energy density solid-state supercapacitors based on porous carbon electrodes derived from pre-treated biowaste precursor sugarcane bagasse. *J. Energy Storage* **55**, 105421 (2022).
26. M. Santhosh, N. et al. Widening the limit of capacitance at high frequency for AC line-filtering applications using aqueous carbon-based supercapacitors. *Carbon* **203**, 686–694 (2023).